Comput. Methods Appl. Mech. Engrg. 417 (2023) 116419

Contents lists available at ScienceDirect

Comput. Methods Appl. Mech. Engrg.

journal homepage: www.elsevier.com/locate/cma

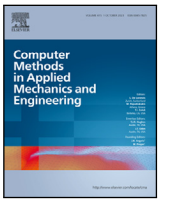

A novel approach to compute the spatial gradients of enriching functions in the X-FEM with a hybrid representation of cracks

Chuanqi Liu *, Yujie Wei

State Key Laboratory of Nonlinear Mechanics, Institute of Mechanics, Chinese Academy of Sciences, Beijing, 100090, China

ARTICLE INFO

Keywords:
X-FEM
Level sets
Hybrid representation
WENO

ABSTRACT

The eXtended Finite Element Method (X-FEM) is a versatile technique to model discontinuities by enriching the trial functions with a prior solution. In the X-FEM, a crack can be explicitly represented by a set of triangles or implicit signed distances, i.e., level set functions, of the points of interest from the crack surface and the crack front. In the explicit representations, it is crucial to accurately evaluate surface normal, conormal, and tangent vectors along crack fronts for computations of the gradients of the enriching functions. The solution is very sensitive to these directional vectors, especially for non-planar 3D cracks. We here propose a novel approach to compute these gradients without evaluating the directional vectors. Level set functions are first set up in a hexahedral grid independent of the background mesh in the X-FEM. We can thus implement the Weight Essentially Non-Oscillatory (WENO) scheme to compute the gradients of level sets. The gradients of the enriching functions at any integration point can therefore be computed by interpolations and chain rules. We compare the implementation procedures of the explicit representation and the proposed hybrid representation in detail. A three-dimensional lens crack problem is studied to demonstrate the accuracy of the proposed method, especially for coarse meshes.

1. Introduction

The accurate modeling of three-dimensional cracks in finite bodies has been studied for decades. This can be achieved by either embedding strong discontinuity in the interpolated displacement field or via a smeared crack approach where a continuous indicator function is used to approximate the sharp discontinuity [1]. The X-FEM and the Generalized Finite Element Method (GFEM) belong to the first strategy. These two methods are synonymous [2] and both rely on the partition-of-unity enrichment to enrich the displacement field [3]. This advance leads to the modeling of arbitrary discontinuities independent of the mesh without requiring remeshing [4]. The essence of the X-FEM is to extend the space of approximation functions with typical functions obtained from analytical solutions for displacements at crack tips. Computing the element stiffness matrix requires calculating the spatial gradients of these enrichment functions. Typically, crack front coordinate systems are used to transform the spatial gradients between local and global systems. Thus, computing the directional vectors at crack fronts appears significant, and it depends on the representation of the cracks. Generally, there are three approaches for representing three-dimensional cracks.

1. Explicit approaches: the crack front and the crack surface are represented explicitly as a mesh [5–9]. For a three-dimensional crack, the surface is typically represented by a polygon partitioned into triangles, so the crack front consists of line segments. With this technique, the crack surface is explicitly meshed separately from the volume mesh. Therefore, the size of the elements in the volume mesh does not affect the accuracy of the crack surface representation, nor does the facet size in the

* Corresponding author.
E-mail address: chuanqil@imech.ac.cn (C. Liu).

https://doi.org/10.1016/j.cma.2023.116419
Received 10 May 2023; Received in revised form 29 August 2023; Accepted 29 August 2023
Available online 13 September 2023

explicit crack surface mesh affect the discretized problem size [10]. Furthermore, the explicit triangular facet representation of the crack surface can preserve special features like kinking and twisting throughout crack growth simulation, and the resulting update of the crack description is straightforward and can be done exactly [8]. However, coupling the purely explicit crack description with the X-FEM is not readily available, particularly because intersecting the crack and model meshes is challenging [11].

2. Implicit approaches: the level set method (LSM) was proposed as an alternative crack representation [6,8,12–14]. The principle of the method is to represent an interface by a zero value of a level set function that gives the signed distance from points to a surface. Since a crack is an inner boundary that does not separate the domain into two regions, a single level set function is not enough to represent a crack and thus an extension of the LSM is commonly used. Consequently, at least two orthogonal level set functions are necessary to represent a crack - one for the crack surface extension, and another orthogonal to the extended surface to locate the crack front [6]. Three level sets can also be used to represent the crack geometry [15]. Level sets address the key X-FEM issue of "where and how to enrich", and simplify implementation. Then, realizing a propagation step requires a model for the update of the level-set function. Such models are rather less intuitive as they often introduce virtual velocity fields and solve Hamilton–Jacobi equations [16,17]. The zero level set must not be updated behind fronts, since cracked points remain cracked. Updating is error-prone, with increments potentially misrepresented [14].
3. Hybrid (explicit–implicit) approaches: the surface is represented by level set nodal values, but evolution is performed explicitly, avoiding solving the evolution equation [11,18–20]. This combines representations, utilizing the strengths of each and covering weaknesses. The explicit localized crack description prevents the implicit representation from creating spurious surfaces. The implicit representation provides local coordinates and easily identifies cut elements [10].

Computing the directional vectors at crack fronts is different for different approaches. For explicit representations, since the surface explicitly presented by facets is C^0, it is non-trivial to compute the base vectors at crack front vertices. For a specific vertex, using the average normal of the facets sharing it may lead to inaccurate estimates, especially for coarse meshes or near geometric singularities [21]. Jiao [22] proposed an eigenvalue analysis of the offset quadric and used it for improved normal computations. A detailed procedure to accurately evaluate the surface normal, conormal and tangent vectors along crack fronts in explicit crack surface representations based on the Face Offsetting Method (FOM) is in [23]. For implicit and hybrid representations, directional vectors can be computed by taking gradients of level sets [7]. When applying the X-FEM for curved cracks, a paradox arises from the mismatch between how we compute the spatial gradients and how we define the enriching functions. Specifically, the enrichments follow an asymptotic field derived for straight cracks using polar (r, θ) coordinates. To match the actual curved geometry, θ must account for curvature rather than just local Cartesian coordinates. However, we still calculate the spatial gradients based on those Cartesian coordinates tied to the crack tip. This disconnect between the Cartesian gradients and polar enrichments creates an implementation challenge unique to the X-FEM for curved cracks. We here introduce an independent hexahedral grid defining level sets and compute the gradients of these level sets based on the Weight Essentially Non-Oscillatory (WENO) scheme [24] to directly compute the gradients of the enriching functions, abandoning the transformations between local and global coordinates. This is beneficial for modeling non-planar cracks. Other issues of implementing the X-FEM are also reviewed as follows for completeness. Stress Intensity Factors (SIFs) are fundamentally important parameters for linear fracture mechanics problems. There are several approaches for the extraction of SIFs from numerical approximations of the solution. Extraction methods based on energy release rate concepts include J-integral [25], the Interaction Integral Method (IIM) [26], the Contour Integral Method (CIM) [27], and the Cutoff Function Method (CFM) [28]. These methods are accurate since theoretically they converge at the same rate as the strain energy [29]. Another class of extraction methods is based on the asymptotic expansion of the elasticity solution in the neighborhood of a crack. This includes the Displacement Correlation Method (DCM) [30] and the stress correlation method [31]. These methods recently have been adopted to extract SIFs from X-FEM solutions [32,33]. The accuracy and convergence of the X-FEM has also been improved by techniques, such as high-order elements [34–36], global–local enrichments [37], high-order singular enriching functions [38,39], etc. In this work, we focus on the representation of cracks and take full advantage of level sets to alleviate the difficulties of computing base vectors for the transformations of global–local coordinates. Therefore, we only implement linear elements with low-order singularity enriching functions and use the DCM to compute SIFs for simplicity. Section 2 briefly reviews the algorithm of the X-FEM. Section 3 presents the proposed algorithm to compute the gradients. Section 4 gives the details of the implementation. Section 5 demonstrates the results. Section 6 concludes the paper with remarks. The code is primarily developed using the deal.II finite element libraries [40,41]; the facets related algorithms are implemented by the Computational Geometry Algorithms Library (CGAL) [42,43]; and we adopt the open-source code "Level Set Method Library (LSMLIB)" to conduct level set operations [44].

2. X-FEM framework for modeling three-dimensional non-planar cracks based on level sets

We first review the basic concepts and formulas in Linear Elastic Fracture Mechanics (LEFM) for clarity. We then give the approximation of displacements in the X-FEM. The definition of level set and its application to represent cracks are also briefly reviewed. Finally, we point out the modifications for computing radial coordinates of three-dimensional non-planar cracks.

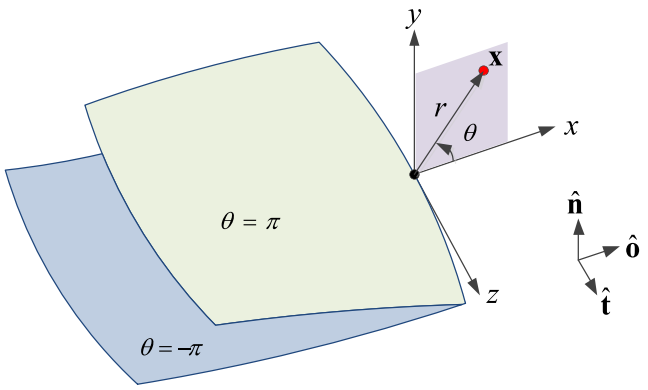

Fig. 1. Local coordinate systems at a crack front vertex. The unit vector $\hat{\boldsymbol{t}}$ is defined in the tangential direction along the local crack front curvature. The unit vector $\hat{\boldsymbol{n}}$ is defined normal to the local crack surface. The unit vector $\hat{\boldsymbol{o}}$ is defined orthogonal to the plane containing $\hat{\boldsymbol{n}}$ and $\hat{\boldsymbol{t}}$.

2.1. Reviews of linear elastic fracture mechanics

As shown in Fig. 1, we define a local Cartesian coordinate system at a crack front vertex. The unit vector along the z-axis is denoted as $\hat{\boldsymbol{t}}$ and is defined in the tangential direction to the local crack front curvature. The unit vector along the y-axis is denoted as $\hat{\boldsymbol{n}}$ and is defined in the normal direction to the local crack surface. The unit vector along the x-axis is denoted as $\hat{\boldsymbol{o}}$ and is defined orthogonal to the plane of $y-z$. As a convention, we also define a polar coordinate system in the plane of $x-y$. The above surface of the crack thus can be represented as $\theta=\pi$, and below surface as $\theta=-\pi$. In the case of a homogeneous and isotropic material, the analytical expressions for the displacement at any point $\boldsymbol{x}(r,\theta)$ in the vicinity of the crack tip are given by Anderson [45]:

$$u_x(r,\theta)=\frac{K_{\mathrm{I}}}{2\mu}\sqrt{\frac{r}{2\pi}}\cos\frac{\theta}{2}\left(\kappa-\cos\theta\right)+\frac{K_{\mathrm{II}}}{2\mu}\sqrt{\frac{r}{2\pi}}\sin\frac{\theta}{2}\left(2+\kappa+\cos\theta\right), \tag{1a}$$

$$u_y(r,\theta)=\frac{K_{\mathrm{I}}}{2\mu}\sqrt{\frac{r}{2\pi}}\sin\frac{\theta}{2}\left(\kappa-\cos\theta\right)+\frac{K_{\mathrm{II}}}{2\mu}\sqrt{\frac{r}{2\pi}}\cos\frac{\theta}{2}\left(2-\kappa-\cos\theta\right), \tag{1b}$$

$$u_z(r,\theta)=\frac{2K_{\mathrm{III}}}{\mu}\sqrt{\frac{r}{2\pi}}\sin\frac{\theta}{2}, \tag{1c}$$

where K_i $(i=I,II,III)$ represents the SIFs for three fracture modes, μ is the shear modulus, $\kappa=3-4\nu$, and ν is the Poisson's ratio. Note that we stay under the assumption of plane strain along the direction tangent to the crack front as the basis for the displacement field. This hypothesis is valid everywhere along the crack front except in the region very close to the skin of the body, as discussed in [46].

2.2. Displacement approximation in the X-FEM

The X-FEM provides a simple and efficient treatment of cracks where the element topologies do not conform to the crack geometry. Some elements are split by the crack and others contain the crack tips. Nodes whose support is bisected by a crack are collected in $\mathcal{N}_{\mathrm{cr}}$, while nodes whose support contains the tips are grouped in $\mathcal{N}_{\mathrm{tip}}$. The crack is represented in the X-FEM by enriching the standard displacement approximation, as follows Sukumar et al. [5]:

$$\boldsymbol{u}^h(\boldsymbol{x})=\sum_{I\in\mathcal{N}}N_I(\mathbf{x})\boldsymbol{u}_I+\sum_{J\in\mathcal{N}_{\mathrm{cr}}}\tilde{N}_J(\boldsymbol{x})\left[H(\boldsymbol{x})-H\left(\boldsymbol{x}_J\right)\right]\boldsymbol{a}_J+\sum_{K\in\mathcal{N}_{\mathrm{tip}}}\tilde{N}_K(\boldsymbol{x})\sum_{\alpha=1}^{4}\left[B_\alpha(\boldsymbol{x})-B_\alpha\left(\boldsymbol{x}_K\right)\right]\boldsymbol{b}_{\alpha K}, \tag{2}$$

where $N_I(\mathbf{x})$ and $\tilde{N}_J(\boldsymbol{x})$ are finite element shape functions, while $\boldsymbol{u}_I$, $\boldsymbol{a}_J$, and $\boldsymbol{b}_{\alpha K}$ are the displacement and enrichment nodal variables, respectively. We here adopt the same shape functions for $N_I(\mathbf{x})$ and $\tilde{N}_J(\boldsymbol{x})$, although they can be different. $H(\boldsymbol{x})$ is the modified Heaviside function which takes on the value $+1$ above the crack and -1 below the crack, and B_α is a basis spanning the asymptotic field near the crack tip:

$$\left[B_1,B_2,B_3,B_4\right]=\left[\sqrt{r}\sin\frac{\theta}{2},\sqrt{r}\cos\frac{\theta}{2},\sqrt{r}\sin\frac{\theta}{2}\sin\theta,\sqrt{r}\cos\frac{\theta}{2}\sin\theta\right]. \tag{3}$$

Note that the enrichment basis functions differ from the formulas for the asymptotic displacement field near the crack tip shown in (1a)–(1c). However, the open-source X-FEM library OpenXFEM++ employs the exact displacement formulas as enrichment functions [47]. It should be pointed out that they are essentially equivalent after transformations.

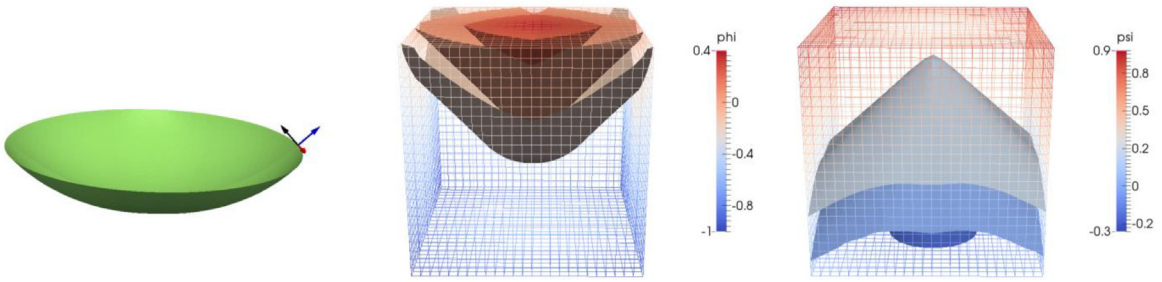

Fig. 2. The geometry of a lens-shaped crack and the coordinate system defined at crack front, and the level sets ϕ and ψ.

2.3. Level set and its application to represent a crack

A level set $\phi(\boldsymbol{x})$ is expressed in the Eulerian coordinates to implicitly represent boundary surfaces. For an extended surface cut the domain, we define $\phi(\boldsymbol{x})$ at a spatial point $\boldsymbol{x}$ as:

$$\phi(\boldsymbol{x}) = \text{sign}\,(\boldsymbol{n}\cdot(\boldsymbol{x}-\bar{\boldsymbol{x}}))\min_{\bar{\boldsymbol{x}}\in\Gamma_c^{\text{ext}}}\|\boldsymbol{x}-\bar{\boldsymbol{x}}\|, \tag{4}$$

where $\boldsymbol{n}$ is the outward normal to the extended crack surface Γ_c^{ext}. Since the crack surface Γ_c is a bounded surface with a crack front, it is also necessary to represent the crack front geometry. Similarly, we define another level set function $\psi(\boldsymbol{x})$. The zero level set of ψ is the surface that passes through the crack front and is orthogonal to the crack surface level set $\phi(\boldsymbol{x}) = 0$ everywhere along the crack front. ψ is calculated as:

$$\psi = \text{sign}\times\sqrt{r^2-\phi^2}, \tag{5}$$

where sign is positive if the point $\boldsymbol{x}$ is in the same direction as the unit vector $\hat{\boldsymbol{o}}$, or negative if in the opposite direction. r represents the shortest distance of the point $\boldsymbol{x}$ to the crack front. The intersection of the surfaces $\phi(\boldsymbol{x}) = 0$ and $\psi(\boldsymbol{x}) = 0$ defines the crack front geometrically. We define the sign of ψ such that the region satisfying $\phi(\boldsymbol{x}) = 0$ and $\psi(\boldsymbol{x}) < 0$ corresponds to the crack surface Γ_c. In practical, the crack is discretized using C^0 continuous triangles. The extension direction is defined as $\hat{\boldsymbol{o}} = \hat{\boldsymbol{t}}\times\hat{\boldsymbol{n}}$, where $\hat{\boldsymbol{t}}$ and $\hat{\boldsymbol{n}}$ are tangent and normal unit vectors at the crack front, as shown in Fig. 1. There exist schemes like FOM [23] to compute $\hat{\boldsymbol{t}}$ and $\hat{\boldsymbol{n}}$ at the front. However, the level set construction is not sensitive to the exact values. For simplicity, we adopt the averaging scheme from [48] to approximate $\hat{\boldsymbol{t}}$ and $\hat{\boldsymbol{n}}$.

$$\boldsymbol{t} = \frac{\sum_i \boldsymbol{t}_i l_i}{\sum_i l_i}, \quad \hat{\boldsymbol{t}} = \frac{\boldsymbol{t}}{\|\boldsymbol{t}\|}, \quad \boldsymbol{n} = \frac{\sum_j \boldsymbol{n}_j a_j}{\sum_i a_j}, \quad \hat{\boldsymbol{n}} = \frac{\boldsymbol{n}}{\|\boldsymbol{n}\|}, \tag{6}$$

where l_i is the length of ith edge connected to the vertex, and a_j is the area of the triangles connected to the vertex. The resulting intersection points and the original nodes on the crack front are triangulated to generate the extended crack surface. The computation of level set ϕ is straightforward using the shortest signed distance to a series of triangles, and the level set ψ is computed using the shortest signed-distance to a set of line segments (composing the crack front) and ϕ. As mentioned before, we utilize the CGAL to calculate the shortest distance to a set of triangles and line segments based on AABB trees [49]. Fig. 2 shows level sets defined on a hexahedral grid for a lens-shaped crack.

2.4. Modifications for three-dimensional curved cracks

It is noteworthy that the asymptotic displacement field is derived for straight cracks using polar coordinates (r,θ) within a plane. We reiterate that the above surface of the crack should be represented as $\theta = \pi$, and below surface as $\theta = -\pi$. This means that the θ coordinate must be defined so that the discontinuity from the displacement field matches the actual curved crack geometry. For curved cracks, computing θ from a local Cartesian coordinate system at the tip, as shown in Fig. 1, would introduce a mismatch between the enrichment discontinuity and the true discontinuity from the curvature. Such inconsistency may severely reduce the accuracy and convergence of the X-FEM. The determination of the plane must also be done carefully for three-dimensional problems. To account for the curvature of curved cracks, we require to rely on level sets even for explicit representations. Based on the level set functions ϕ and ψ defined in Eqs. (4) and (5), the polar coordinates (r,θ) can be computed as:

$$r(\boldsymbol{x}) = \sqrt{\phi^2(\boldsymbol{x})+\psi^2(\boldsymbol{x})}, \quad \theta = \text{atan2}(\phi,\psi), \tag{7}$$

where atan2 returns the principal value of the arc tangent of ϕ/ψ taking into account the sign of both arguments to determine the quadrant. Fig. 3 compares the computed θ/π using different methods for a lens-shaped crack within a cube. This allows us to account for the curvature of the crack.

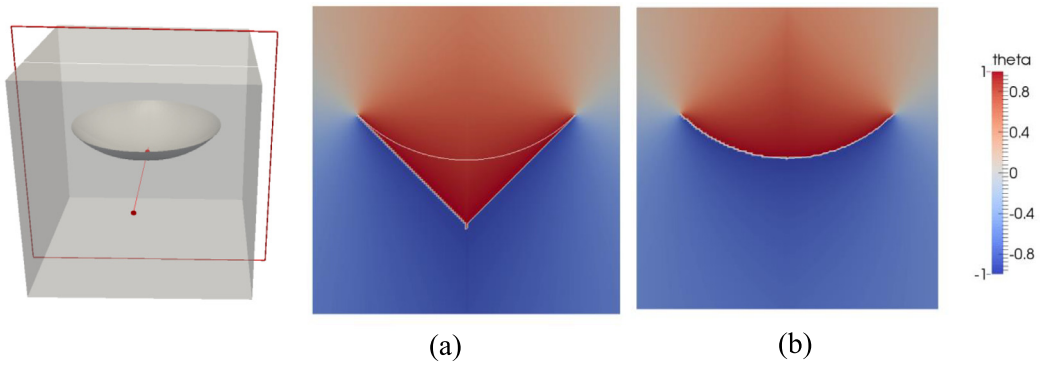

Fig. 3. Comparison of θ/π computed using different methods for a lens-shaped crack within a cube: (a) determined directly from local Cartesian coordinates at the crack tip, and (b) the modified approach accounting for crack curvature based on level set functions.

3. New spatial gradients computation algorithm and comparison to common approach

Previously, after determining (r,θ), local Cartesian systems at each point along the curved crack front were constructed to transform to the global coordinate system. However, for points sharing the same closest position on the front, the local systems can vary point-to-point, which is non-physical. To address this, we introduce using the chain rule to directly compute the gradients of enriching functions, eliminating the need to compute local base vectors at the crack front. In this section, we first outline two approaches for computing the gradients of enriching functions. We then review the scheme for computing base vectors in explicit crack representations and describe our proposed model in detail.

3.1. Spatial gradients of enriching functions

When generating the stiffness matrix, it is necessary to compute the gradients of the enriching functions. The formula of the stiffness matrix in the X-FEM can be found in [5]. Using the chain rule, the gradients of singular functions along ith axis are

$$B_{\alpha,i} = \frac{\partial B_\alpha}{\partial r}\cdot\frac{\partial r}{\partial x_i} + \frac{\partial B_\alpha}{\partial \theta}\cdot\frac{\partial \theta}{\partial x_i}, \quad \alpha = 1,2,3,4, \quad i = 1,2,3, \tag{8}$$

where x_i is the global coordinates. Considering (8), we can compute $\partial B_\alpha/\partial r$ and $\partial B_\alpha/\partial\theta$ as shown in Appendix A. To compute $\partial r/\partial x_i$ and $\partial\theta/\partial x_i$, we have two options.

1. computation based on transforming between the global and local coordinate systems. It follows

$$\frac{\partial r}{\partial x_i} = \frac{\partial r}{\partial X_j}\frac{\partial X_j}{\partial x_i}, \quad \frac{\partial \theta}{\partial x_i} = \frac{\partial \theta}{\partial X_j}\frac{\partial X_j}{\partial x_i}, \tag{9}$$

where the Einstein summation convention is adopted for the repeated j, X_j is the local Cartesian coordinates as shown in Fig. 1, and $\partial X_j/\partial x_i$ is the Jacobian matrix. We have:

$$\frac{\partial r}{\partial X_1} = \cos\theta, \quad \frac{\partial r}{\partial X_2} = \sin\theta, \quad \frac{\partial r}{\partial X_3} = 0, \tag{10}$$

$$\frac{\partial \theta}{\partial X_1} = -\frac{\sin\theta}{r}, \quad \frac{\partial \theta}{\partial X_2} = \frac{\cos\theta}{r}, \quad \frac{\partial \theta}{\partial X_3} = 0. \tag{11}$$

Considering that

$$\begin{bmatrix} X_1 \\ X_2 \\ X_3 \end{bmatrix} = \begin{bmatrix} o_1 & o_2 & o_3 \\ n_1 & n_2 & n_3 \\ t_1 & t_2 & t_3 \end{bmatrix}\begin{bmatrix} x_1 \\ x_2 \\ x_3 \end{bmatrix} \Rightarrow \frac{\partial X_i}{\partial x_j} = \begin{bmatrix} o_1 & o_2 & o_3 \\ n_1 & n_2 & n_3 \\ t_1 & t_2 & t_3 \end{bmatrix}, \tag{12}$$

we can see that the base vectors are significant for the accuracy of this scheme.

2. computation based on the spatial gradients of level sets. Since (r,θ) are computed via ϕ and ψ as shown in (7), we further have:

$$\frac{\partial r}{\partial x_i} = \frac{\partial r}{\partial \phi}\cdot\frac{\partial \phi}{\partial x_i} + \frac{\partial r}{\partial \psi}\cdot\frac{\partial \psi}{\partial x_i}, \quad \frac{\partial \theta}{\partial x_i} = \frac{\partial \theta}{\partial \phi}\cdot\frac{\partial \phi}{\partial x_i} + \frac{\partial \theta}{\partial \psi}\cdot\frac{\partial \psi}{\partial x_i}, \tag{13}$$

where

$$\frac{\partial r}{\partial \phi} = \frac{\phi}{\sqrt{\psi^2+\phi^2}}, \quad \frac{\partial r}{\partial \psi} = \frac{\psi}{\sqrt{\psi^2+\phi^2}}, \quad \frac{\partial \theta}{\partial \phi} = \frac{\psi}{\psi^2+\phi^2}, \quad \frac{\partial \theta}{\partial \psi} = -\frac{\phi}{\psi^2+\phi^2}. \tag{14}$$

We thus only need to compute the spatial gradients of level sets.

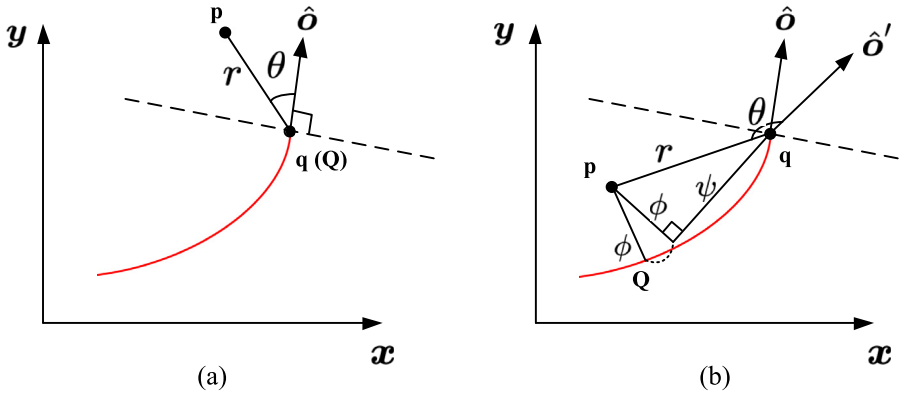

Fig. 4. Definition of θ for a curved crack and the base vectors for the given point p.

In the following, we separately describe the computation of base vectors at the crack front for scheme 1 and spatial gradients of level sets for scheme 2.

3.2. Computation of base vectors at the crack front

For a given point **p**, we first compute the closest point **q** on the crack fronts, and the closest point **Q** on the crack surface. Once the location of **q** is determined, we can compute the corresponding Cartesian coordinate system as shown in Fig. 1. The relative position of **p** and the $y-z$ plane can be determined by comparing the area of the triangle **pqQ** to a prescribed tiny value. If the area is smaller (the point q coincides with the point Q), which means the point **p** is in the positive half-space of the plane $y-z$ as shown in Fig. 4(a), θ is simply the angle between **qp** and $\hat{o}$. Otherwise, the polar coordinates (r,θ) are constructed within the plane, i.e. x–y plane, determined by **pqQ**, as shown in Fig. 4(b). Note that θ is computed via (7). Once θ is determined, we can reconstruct a local Cartesian system with three unit vectors, $\hat{o}'$, $\hat{t}'$, and $\hat{n}'$. This system is used for the computation of the gradients of r and θ. For the case shown in Fig. 4(a), the coordinate system does not change. However, for the case shown in Fig. 4(b), the $\hat{t}'$ is determined by the normal vector of the triangle **pqQ**. We then require to rotate the vector **pq** along the axis directed by $\hat{t}'$ with $-\theta$ to compute $\hat{o}'$. The rotation matrix for such a 3D rotation is:

$$R(\hat{\boldsymbol{t}},\theta)=\begin{pmatrix}\cos\theta+t_1^2(1-\cos\theta) & t_1t_2(1-\cos\theta)-t_3\sin\theta & t_1t_3(1-\cos\theta)+t_2\sin\theta\\ t_1t_2(1-\cos\theta)+t_3\sin\theta & \cos\theta+n_2^2(1-\cos\theta) & t_2t_3(1-\cos\theta)-t_1\sin\theta\\ t_1t_3(1-\cos\theta)-t_2\sin\theta & t_2t_3(1-\cos\theta)+t_1\sin\theta & \cos\theta+t_3^2(1-\cos\theta)\end{pmatrix}, \tag{15}$$

where $\hat{t}'=(t_1,t_2,t_3)$. The $\hat{n}'$ can be computed as: $\hat{n}'=\hat{o}'\times\hat{t}'$. We therefore can compute the gradients of enriching functions via (9)–(12).

3.3. Gradients of level sets computed by the finite-difference method for a hexahedral grid

As shown in (13), we can directly compute the gradients of enriching functions without calculating the base vectors if we know the gradients of level sets. For the hybrid representation, people normally compute level sets at nodes of the same body mesh resulting that the accuracy of the crack surface representation is mesh dependent [7]. Obviously, we thus can compute the gradients of level sets using the gradients of nodal shape functions. However, this accuracy is highly dependent on the order of the element and the cell size of the grid. To improve accuracy, we introduce an independent hexahedral grid defined of level sets and compute the gradients of level sets based on the finite difference method, e.g. the WENO scheme [24] to discretize the spatial gradients to fifth-order accuracy. As shown in Fig. 5, the studied domain is discretized into blue cells. It is required to the compute the gradients of enriching functions at the integration point, e.g. the blue circle in the figure. Instead of defining level sets on the same grid for the physical domain, we define level sets on a separate spatial domain discretized by the red hexahedral cells. Note that the spatial domain defined with level sets does not need to coincide with the physical domain and only needs to be set at the vicinity of the front of the crack. Relying on the regular grid defined with level sets, we can compute the gradients of level sets at nodes of the grid with high accuracy. We here adopt the WENO scheme and review the algorithm briefly for completeness. More details can be found in [50]. The backward difference approximation to the derivative is defined as:

$$(D^-\phi)_i=\frac{\phi_i-\phi_{i-1}}{\Delta x}, \tag{16}$$

where Δx is the mesh spacing. Defining $v_1=D^-\phi_{i-2}$, $v_2=D^-\phi_{i-1}$, $v_3=D^-\phi_i$, $v_4=D^-\phi_{i+1}$, and $v_5=D^-\phi_{i+2}$ allows us to write

$$\phi^1_{,x}=\frac{v_1}{3}-\frac{7v_2}{6}+\frac{11v_3}{6},\quad \phi^2_{,x}=-\frac{v_2}{6}+\frac{5v_3}{6}+\frac{v_4}{3},\quad \phi^3_{,x}=\frac{v_3}{3}+\frac{5v_4}{6}-\frac{v_5}{6}, \tag{17}$$

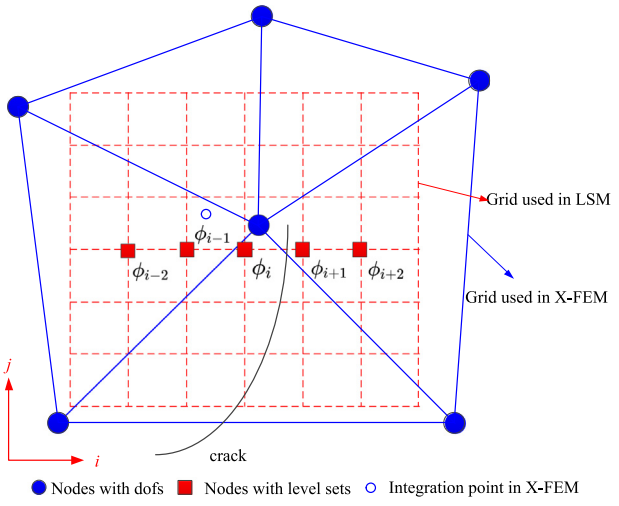

Fig. 5. Dual-meshes for the hybrid representation.

as the three potential ENO approximation to ϕ_x^-. The WENO approximation of $(\phi_{,x}^-)_i$ is a convex combination of the approximation given by

$$\phi_{,x} = \omega_1 \phi_{,x}^1 + \omega_2 \phi_{,x}^2 + \omega_3 \phi_{,x}^3, \tag{18}$$

where the $0 \le \omega_k \le 1$ are the weights with $\omega_1 + \omega_2 + \omega_3 = 1$. The key observation for obtaining high-order accuracy in smooth regions is that weights of $\omega_1 = 0.1$, $\omega_2 = 0.6$ and $\omega_3 = 0.3$ give the optimal fifth-order accurate approximation to $\phi_{,x}$. These optimal weights are derived rigorously in [24,50]. As noted in the original text, the detailed derivations can be found in these references. We adopt these optimal weight values and use the same WENO scheme for the gradients of both $\phi_{,i}$ and $\psi_{,i}$. Note that the integration points for the X-FEM enrichment do not coincide with the nodes of the regular hexahedral grid. We first compute the gradients of the level sets at the nodes using the WENO scheme described previously. To obtain the gradients at the integration points, we interpolate from the nodal values using the shape functions of the enriched X-FEM element. The open-source LSMLIB code in C++ [44] facilitates setting up the level sets and operations on them, so this process is not too cumbersome.

4. Implementation details

In this section, we first describe the implementing procedure as shown in Algorithm 1. The implementation platforms adopted in this work are given for convenience. The integration schemes concentrating on the partitioning are then compared. We lastly illustrate the computation of SIFs.

Algorithm 1 Algorithm to compute the spatial gradients of enriching functions

Require: Triangles $\mathcal{T}$ representing a crack
Ensure: Spatial gradients of enriching functions for a given integration points p, i.e. $B_{\alpha,i}(\boldsymbol{x}_p)$.
Define a structured grid $\mathcal{G}$
Extend $\mathcal{T}$ to cut the domain $\mathcal{G}$ for determining the sign of level sets.
for each vertex v in $\mathcal{G}$ **do**
Compute the shortest signed distance of v to $\mathcal{T}$, i.e. $\phi(\boldsymbol{x}_v)$, according to (4).
Compute the shortest distance of v to the bound of $\mathcal{T}$, i.e. r.
Compute the second level set determining the position of the crack front, i.e. $\psi(\boldsymbol{x}_v)$, according to (5).
Compute the fields of spatial gradients of the level sets, i.e. $\phi_{,i}(\boldsymbol{x})$ and $\psi_{,i}(\boldsymbol{x})$, in a manner of (18).
Obtain the spatial gradients of level sets at the quadrature point using interpolation, $\phi_{,i}(\boldsymbol{x_p}) = \sum_I N_I(\boldsymbol{x}_p)\phi_{,i}(\boldsymbol{x_I})$ and $\psi_{,i}(\boldsymbol{x_p}) = \sum_I N_I(\boldsymbol{x}_p)\psi_{,i}(\boldsymbol{x_I})$.
Compute $\partial r/\partial x_i$ and $\partial\theta/\partial x_i$ by using the chain rule according to (13).
Compute the spatial gradients of enriching functions $B_{\alpha,i}(\boldsymbol{x}_p)$ according to (8).

4.1. Implementation platforms

The main platform to implement the X-FEM is deal.II [40,41]. This library provides the discretization for the study domain, handler of degrees of freedom (DOFs), and versatile linear solvers. Since deal.II is cell-based, we require using "hp::FECollection" to

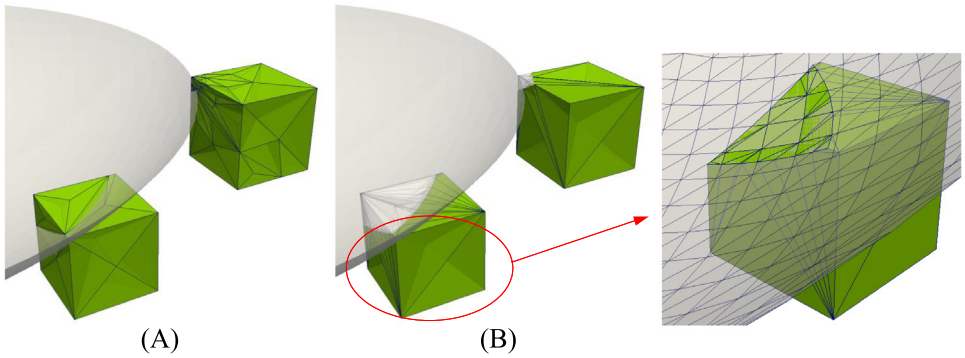

Fig. 6. Comparison of sub-cells partitioned by the crack: (A) hybrid representation, and (B) explicit representation and local zoom.

collect different types of "FESystem" composed by vectors of "FiniteElement". For the element enriched by the singular functions, the vector contains 5 "FE_Q", for the element enriched by the heaviside function contains 2 "FE_Q", and for the unenriched element, the vector only contains 1 "FE_Q". It should noted that the lengths of these vectors must maintain the same in deal.II and we employ "FE_Nothing" for this purpose. In contrast, the number and type of enriching functions are node-based. Therefore, we need to set a vector containing this information for each node. The "constraints" class is employed to constrain the extra DOFs of over-enriched nodes belonging to enriched elements. Other implementation details are straightforward in deal.II. The crack is composed by a series of triangles, and we here adopt the CGAL library [43]. We can redesign our own vertex, border, facet, and items, publicly derived from "HalfedgeDS_vertex_max_base_with_id", "HalfedgeDS_face_max_base_with_id", and "Polyhedron_items_with_id_3", respectively, to contain more information, such as normal vectors. The facets for the crack can thus be stored using "Polyhedron_3". The shortest distance searching is conducted based on the "AABB_tree", and the extension of the crack surface can be done by "Polyhedron_incremental_builder_3". The library for level set is LSMLIB [44]. The level set values are stored in "LSM_DataArrays", and the background grid is specified by a "Grid" class initialized by "createGridSetDx". LSMLIB provides various functions to compute the spatial gradients of level sets, such as "LSM3D_HJ_WENO5", "LSM3D_CENTRAL_GRAD_ORDER2", and more. Users can easily implement these functions.

4.2. Partitioning for elements fully or partly cut by the crack

Integration schemes for elements fully or partly cut by the crack have been widely studied since the development of X-FEM. Although some integration schemes without element-partitioning have been proposed in recent years [51–53], the integration scheme based on element-partitioning remains straightforward. For the hybrid representation, the fully-cut element is partitioned into tetrahedra only according to ϕ. The partly-cut element is first partitioned into tetrahedra according to ϕ, and the tetrahedra may be further partitioned into sub-tetrahedra according to ψ. We set the quadrature points at the centers of the tetrahedra. The partitioning is implemented using open-source code provided by Sukumar [54]. Two representative elements partitioned into tetrahedra for the hybrid representation are illustrated in Fig. 6(A). Note that with this approach, the crack surface is assumed to be planar within each element and the triangulation of the crack surface cannot be considered. For the explicit representation, CGAL provides powerful tools to determine whether a cube is cut by a set of triangles and to partition the element. The function "number_ of_intersected_primitives" is designed to determine the number of the intersected elements in an "AABB_tree". Since the border is composed by line segments stored in an "AABB_tree" and the crack surface composed of facets is also stored in another "AABB_tree", we can readily determine whether a specific cell is by fully or partly cut by the crack. More conveniently, "clip" and "corefine_ and _compute_difference" are functions in the "Polygon_mesh_processing" namespace. Using these two functions, we can partition the fully-cut element into two parts according to the triangulation of the crack. Thus, we can obtain the set of tetrahedra of each part, and set quadrature points for each tetrahedron. Fig. 6(B) shows the tetrahedra, and the zoom subfigure clearly shows that the cutting surface considers the triangulation of the crack.

4.3. Computation of SIFs

Calculating mixed-mode stress intensity factors point-wise along a general 3-D curved crack front with a non-planar crack surface requires a robust numerical method. A domain integral method, such as the interaction integral method (IIM) [55], is gaining popularity due to its general applicability to a wide variety of crack problems. In the IIM, auxiliary fields are introduced and superposed on top of the actual fields from the solution to the boundary value problem. Through suitable definitions of the auxiliary fields, the IIM can be related to the mixed-mode stress intensity factors. However, an accurate computation requires considering the discrepancies between the crack surface (actual fields) and the planar surface (auxiliary fields) determined by the crack front, which complicates the derivations and calculations [56]. Since the computation of SIFs is not the focus of this work, we adopt the

simplest scheme, i.e. DCM, to calculate SIFs. Using the crack front coordinate system defined in Fig. 1 at a fixed value of z, the jump in the $i-$th component of the displacement field across the crack surface is calculated as:

$$[\![u_i(r)]\!] = u_i(r,\pi) - u_i(r,-\pi) \quad i = 1,2,3. \tag{19}$$

The Mode I, II, and III SIFs can then be approximated according to the theoretical solution of the displacement (1a)–(1c)

$$K_I^*(r) = \sqrt{\frac{2\pi}{r}}\frac{G}{\kappa+1}[\![u_2(r)]\!], \quad K_{II}^*(r) = \sqrt{\frac{2\pi}{r}}\frac{G}{\kappa+1}[\![u_1(r)]\!], \quad K_{III}^*(r) = \sqrt{\frac{2\pi}{r}}\frac{G}{4}[\![u_3(r)]\!]. \tag{20}$$

To increase the order of accuracy of (20), we give three different radius $r_a > r_b > r_c$ to extrapolate the SIFs [57] according to

$$K_i = \frac{K_i^*(r_a)\,c_1 + K_i^*(r_b)\,c_2 + K_i^*(r_c)\,c_3}{c_1+c_2+c_3}, \quad i = \mathrm{I},\mathrm{II},\mathrm{III}, \tag{21}$$

with

$$c_1 = r_b r_c^2 - r_b^2 r_c, \quad c_2 = r_c r_a^2 - r_c^2 r_a, \quad c_3 = r_a r_b^2 - r_a^2 r_b. \tag{22}$$

In this work, these three points are uniformly spaced at a distance of Δr, that is, $\Delta r = r_a - r_b = r_b - r_c$. Note that if the crack surface is non-planar in the x direction, we require ensuring that the sampling points are on the crack surface. A simple fix for this, presented in [21], to compute the orthogonal projection of the extraction points onto the curved crack surface. The process is normal, only modifying r_a, r_b, and r_c according to the projected points on the crack surface. It should be pointed out that the accuracy of DCM depends on the locations of monitoring points in our applications. Since we aim to compare the gradients computed by different methods, the dependence of SIFs on the Δr and r_a may confuse the comparison if we take SIFs as criteria. We alleviate this issue by comparing statistic values. More details will be given in the next section.

5. Numerical examples

In this section, we first compare the gradients computed by different schemes at specific spatial points to demonstrate the errors of the method requiring directional vectors. We then present numerical simulations of two boundary value problems to further analyze the accuracy of the different methods: one example involves a planar crack geometry and the other involves a non-planar crack. Both examples have analytical solutions available for validation of the implementation. The planar crack example involves an inclined elliptical crack. We use this example to demonstrate the consistence between the proposed model and the model computing the transformation matrix specifically for planar cracks. The non-planar example involves a spherical cap crack geometry. We employ this example to compare the accuracy of the different methods for modeling non-planar cracks. Note that although the grid of the X-FEM can be tetrahedra as shown in Fig. 5, we here still use hexahedra to discretize the physical domain for convenient implementations in deal.II. Again, the grid for the level set is independent with the meshes for the physical domain, allowing different cell sizes.

5.1. Comparison of different schemes to compute the spatial gradients of enriching functions

In this example, we do not solve a boundary value problem, and just quantitatively compare the spatial gradients of enriching functions (as shown in (8)) computed by different methods. As shown in Fig. 7, we here consider four points with different relative positions to a lens. The lens has a radius of 0.2, the angle between the rotating radial axis and z-axis is $\pi/4$, and the origin is at $(0,0,0.2)$. We use the triangle **pqQ** (defined in Fig. 4) to characterize the relative positions of the interested points. Note that the fourth point $\mathbf{p}_4$ is in the situation as shown in Fig. 4(a), where the closest point at the front of the crack $\mathbf{q}$ coincides with the closest point on the crack surface $\mathbf{Q}$. The triangle therefore shrinks to a line segment in this case. Table 1 compares the gradients of the first two enriching functions computed via different methods. "Explicit" refers to the method based on the transformation matrix, and "Dual" refers to the method based on the gradients of level sets. The first two points are along on the z-axis, therefore $B_{\alpha,x}$ and $B_{\alpha,y}$ should theoretically be zeros. We can see that the proposed method reaches this theoretical value with high accuracy, but the method based on the base vectors is relatively inaccurate since there are always closest points on the surface and front of the crack affecting the gradient computations. Except for this extreme situation, the gradients are also discrepant for $\mathbf{p}_3$. Due to the curvature, we believe that the proposed method is more accurate than the method based on the transformation matrix. When the point is in the out-forward half space of $y-z$ plane, i.e. $\mathbf{p}_4$, the discrepancies become much smaller, meaning the method based on the transformation matrix is more suitable for this situation. We may conclude that the proposed method is more accurate than the method using the transformation matrix for cases where the curvature of the crack plays an important role, such as when a coarse grid embeds a non-planar crack. To some extent, we can improve the accuracy of the X-FEM to describe non-planar cracks for a given number of unknowns using the proposed method.

5.2. Inclined elliptical crack

An elliptical crack embedded diagonally in a cubic domain is studied in this section, which is widely employed for validations [21, 58]. As shown in Fig. 8(a), the domain with length $L = 0.5$ is loaded by a unity tensile traction $\sigma = 1.0$ on two opposite faces of the domain. The dimensions of the semi-major and semi-minor axis of the crack are taken as $a = 0.1$ and $b = 0.05$, respectively,

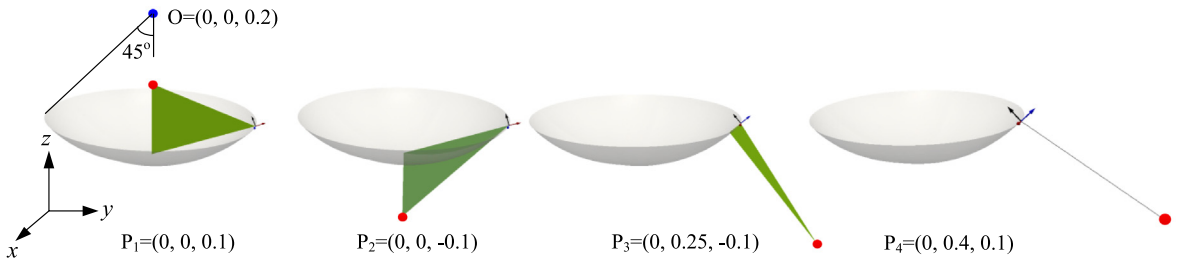

Fig. 7. Four specific spatial positions.

Table 1
Comparison of gradients of enriching functions using different schemes.

	p_1		p_2		p_3		p_4	
	Explicit	Dual	Explicit	Dual	Explicit	Dual	Explicit	Dual
$B_{1,x}$	−1.27865	−1.69e−15	**0.88370**	**8.76e−16**	−0.04908	0.00065	−0.07424	0.01811
$B_{1,y}$	−0.02221	−1.69e−15	**0.15239**	**8.76e−16**	0.13413	−0.04466	−0.10917	−0.10177
$B_{1,z}$	−0.11444	−0.20487	0.61053	0.59333	1.13155	0.97779	**0.89819**	**0.90212**
$B_{2,x}$	**−0.11351**	**−1.13e−16**	0.60165	2.19e−16	−0.05603	0.00075	−0.05863	0.01446
$B_{2,y}$	**−0.01520**	**−1.13e−16**	0.10375	2.19e−16	**1.13095**	**0.92704**	0.89990	0.90212
$B_{2,z}$	1.29780	1.47882	−0.89674	−0.96987	−0.13648	−0.30391	0.10453	0.10178

as shown in Fig. 8(b). The angle of inclination of the crack with respect to the horizontal plane is taken as $\gamma = \pi/4$. The material properties adopted in this problem are $E = 1.0 \times 10^3$ and $\nu = 0.3$. The stress intensity factors K_I^{ref}, K_{II}^{ref} and K_{III}^{ref} for an inclined elliptical crack in an infinite domain are used as reference values. They are given by Tada et al. [59]:

$$K_{\text{I}}^{\text{ref}} = \frac{\left(\sigma \sin^2\gamma\right)\sqrt{\pi b}}{E(\kappa)}\left\{\sin^2\theta + \left(\frac{b}{c}\right)^2\cos^2\theta\right\}^{1/4}, \tag{23}$$

$$K_{\text{II}}^{\text{ref}} = -\frac{(\sigma \sin\gamma\cos\gamma)\sqrt{\pi b}\kappa^2}{\left\{\sin^2\theta + \left(\frac{b}{a}\right)^2\cos^2\theta\right\}^{1/4}}\left\{\frac{\kappa'}{B}\cos\omega\cos\theta + \frac{1}{C}\sin\omega\sin\theta\right\}, \tag{24}$$

$$K_{\text{III}}^{\text{ref}} = \frac{(\sigma \sin\gamma\cos\gamma)\sqrt{\pi b}(1-\nu)\kappa^2}{\left\{\sin^2\theta + \left(\frac{b}{a}\right)^2\cos^2\theta\right\}^{1/4}}\left\{\frac{1}{B}\cos\omega\sin\theta - \frac{\kappa'}{C}\sin\omega\cos\theta\right\}, \tag{25}$$

where B, C are defined as

$$B = \left(\kappa^2 - \nu\right)E(\kappa) + \nu\kappa'^2 K(\kappa), \quad C = \left(\kappa^2 + \nu\kappa'^2\right)E(\kappa) - \nu\kappa'^2 K(\kappa), \tag{26}$$

with $E(\kappa)$ and $K(\kappa)$ defined as

$$K(k) = \int_0^{\frac{\pi}{2}} \frac{d\varphi}{\sqrt{1-k^2\sin^2\varphi}}, \quad E(k) = \int_0^{\frac{\pi}{2}} \sqrt{1-k^2\sin^2\varphi}\, d\varphi, \tag{27}$$

where $\kappa^2 = 1 - \kappa'^2$, $\kappa' = b/a$, and θ is the parametric angle of a point on the crack front. In this problem, $\gamma = \pi/4$ and $\omega = 0$. For the spatial discretization, we employ a structured grid with a uniform cell size of $h_{\text{xfem}} = 0.025$ as the background meshes of the X-FEM, and a uniform grid with cell size of $h_{\text{ls}} = 0.0266667$ for the level set. The region within a distance of $1.5h_{\text{xfem}}$ from the crack front is enriched with singularity functions.

Fig. 9(a) shows a vertically cut half of the deformed body amplified with 500 times. We set $r_a = 0.002$ and $\Delta r = 0.003$ as shown in (22) to compute SIFs. Figs. 9(b), 9(c) and 9(d) compare the SIFs computed by different schemes. We can see that the accuracies of the explicit and the novel hybrid representations are almost identical. This is expected since computing gradients of enriching functions using the transformation matrix and gradients of level sets give identical results for planar cracks.

5.3. Lens-shaped crack

Since the spherical-cap crack problem is the only one non-planar crack for which the boundary-value problem can be solved exactly [60], we consider this case here. As shown in Fig. 10, a lens-shaped crack embedded in a cubic domain. The geometric parameters of the lens-shaped crack are $R = 0.2$ and $\alpha = \pi/4$, and the edge length of the cube is $L = 2$. The material properties used are $E = 1.0 \times 10^3$ and $\nu = 0.22$.

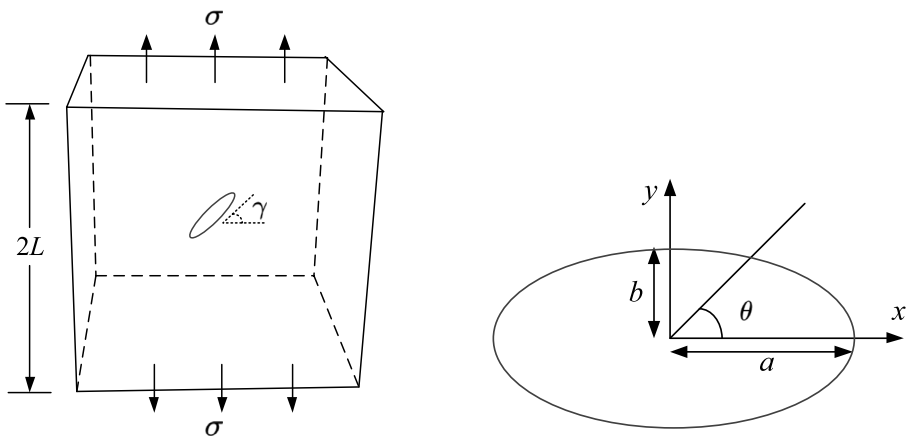

(a) Numerical model **(b)** Geometry of the crack

Fig. 8. Numerical model and the geometry of an elliptical crack.

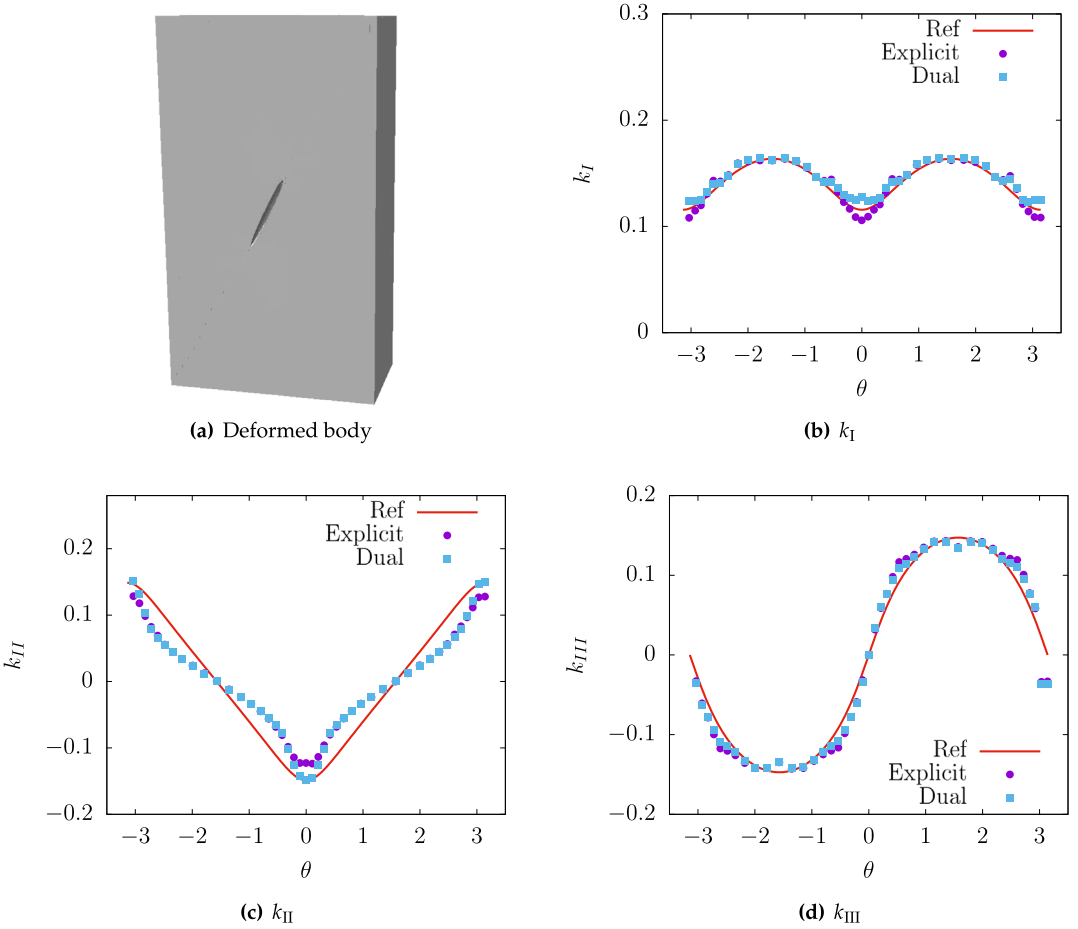

(a) Deformed body **(b)** k_{I} **(c)** k_{II} **(d)** k_{III}

Fig. 9. Deformed body (amplified by 500 times) and comparisons of SIFs (Ref: analytical solution, Explicit: crack represented by an explicit scheme, and Dual: the dual meshes approach).

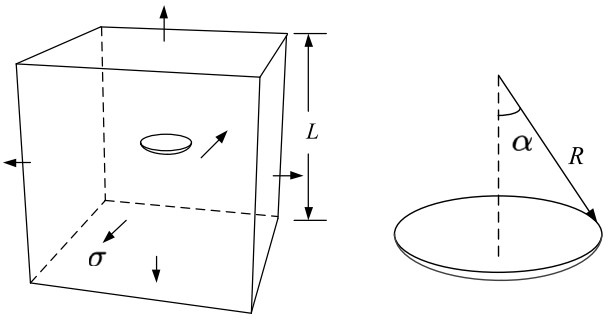

(a) Numerical model **(b)** Geometry of the crack

Fig. 10. Numerical model and the geometry of a lens crack.

5.3.1. Comparisons of SIFs computed by the DCM

When the domain subjected to a hydrostatic tensile stress, i.e. $\sigma = 1$, the fairly involved analytical solution for the lens crack was derived by Martynenko and Ulitko [61]. The stress intensity factors are given by:

$$K_{\mathrm{I}}^{\mathrm{ref}} = \frac{\varphi(\alpha)}{2}\sqrt{\frac{R\pi}{\sin\alpha}} \quad \text{and} \quad K_{\mathrm{II}}^{\mathrm{ref}} = \psi(\alpha)\sqrt{\frac{R\pi}{\sin\alpha}}, \tag{28}$$

where $\varphi(\alpha)$ and $\psi(\alpha)$ are solutions to the boundary value problem of a spherical notch, which can be expressed as:

$$\varphi(\alpha) = \delta \sin\frac{\alpha}{2} + b\sin\frac{3\alpha}{2} + c\sinh\gamma\alpha\cos\frac{\alpha}{m} + d\cosh\gamma\alpha\sin\frac{\alpha}{m}, \tag{29}$$

$$\psi(\alpha) = \frac{2b}{3}\cos\frac{3\alpha}{2} - \frac{1}{6}(c\eta + 2d\gamma)\sinh\gamma\alpha\sin\frac{\alpha}{m} - \frac{1}{6}(2c\gamma - \eta d)\cosh\gamma\alpha\cos\frac{\alpha}{m}, \tag{30}$$

in which m is the reciprocal of Poisson's ratio and the constants δ, γ, and η are defined as

$$\delta = \frac{3\sigma}{2\pi}\frac{m}{m+1}, \quad \gamma = \sqrt{\frac{3}{4} - \frac{1}{m^2}}, \quad \eta = 3 + \frac{2}{m}. \tag{31}$$

The remaining constants b, c, and d are determined from a solution of the following equation system:

$$\begin{bmatrix} a_{11} & -a_{12} & -a_{13} \\ a_{21} & -a_{22} & -a_{23} \\ a_{31} & -a_{32} & -a_{33} \end{bmatrix} \begin{pmatrix} b \\ c \\ d \end{pmatrix} = -\delta \begin{Bmatrix} b_{11} \\ b_{22} \\ 0 \end{Bmatrix} \tag{32}$$

in which the coefficients a_{ij} and b_{ij} are given in Appendix. In this case, the absolute values of analytical solutions are $K_{\mathrm{I}}^{\mathrm{ref}} = 0.377235$, $K_{\mathrm{II}}^{\mathrm{ref}} = 0.104089$, and $K_{\mathrm{III}}^{\mathrm{ref}} = 0$. We first set $h_{\mathrm{xfem}}/L = 0.03125$ and $h_{\mathrm{ls}}/L = 0.05$ for the spatial discretization. We also set $r_a = 0.01414$ and $\Delta_a = 0.05656$ shown in (22) to compute SIFs. Fig. 11 shows comparisons of SIFs computed by different methods and the analytical solutions. Note the x-axis denoted as θ is defined as the radial angle of the points along the crack front in the horizontal plane. We can see that the computed SIFs from both methods fluctuate around the reference solutions. Given a fixed singularly-enriched region, the curvature plays an important role for coarse meshes. We therefore employ coarse meshes to discretize the domain to examine the improvement of the proposed method. As shown in Fig. 12, two representative cell sizes are demonstrated by the relative positions of the cells cut by the crack front and the crack itself.

We now compare SIFs for different approaches. Since the SIFs computed by the DCM method are practically path dependent. We here first separately compute k_{I} with $r_a = 0.0002828 + ih_{\mathrm{cr}}$ and $\Delta_a = 0.0002828 + jh_{\mathrm{cr}}$ $(i, j = 1, 2, \ldots, 10)$ and take the average k_{I} to eliminate the issue of path-dependence. Fig. 13 shows the relative error $e_k = \left|k_{\mathrm{I}} - k_{\mathrm{I}}^{\mathrm{ref}}\right| / k_{\mathrm{I}}^{\mathrm{ref}}$ with different mesh sizes for the different methods. We can see that the proposed method is more accurate than the method based on the transformation matrix for coarse meshes, but for a few specific mesh sizes, the results are worse. The reason is that the computation of SIFs by using the DCM is not accurate even when we use some averaging schemes. The interaction integral method (IIM) considering the discrepancies of the crack surface (actual fields) and the planar surface (auxiliary fields), may be a better choice, as shown in [55]. However, the derivations and implementations of the IIM for a curved crack are too complicated, which may distract from the focus of this work. To conduct a fair comparison, we employ the analytical solution for the displacement jump along the lens.

5.3.2. Comparisons of displacement jump

Martin [60] revisited the spherical-cap crack and given the analytical crack-opening displacement for uniaxial tension at infinity in the z-direction as:

$$\left[u_r(\theta)\right] = c\int_{\theta}^{\alpha} \frac{\varphi(t)}{\sqrt{2\cos\theta - 2\cos t}}\,\mathrm{d}t, \quad 0 \le \theta < \alpha, \tag{33}$$

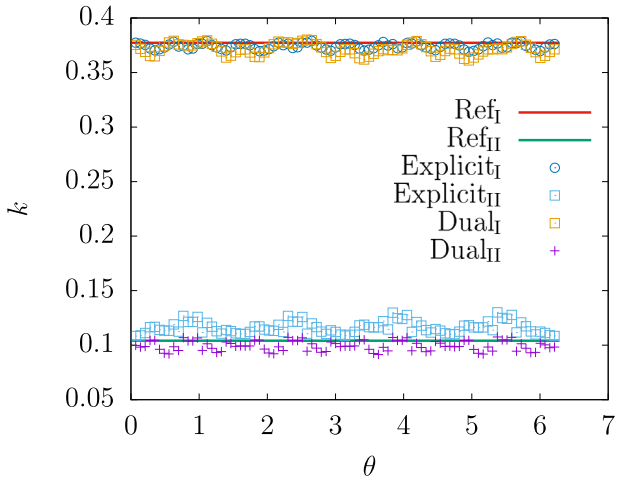

Fig. 11. SIFs for a lens crack (Subscripts I and II represent the K_I and K_{II}, respectively. Ref: analytical solution, Explicit: crack represented by an explicit scheme, and Dual: the dual meshes approach.).

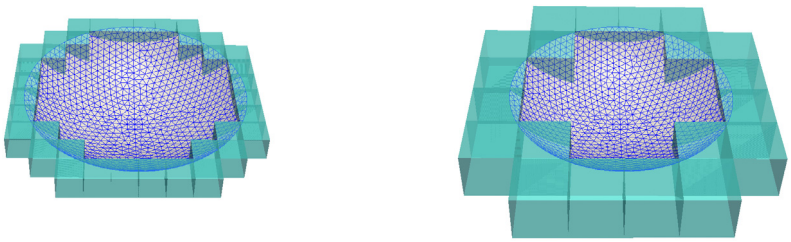

(a) $h_{xfem}/L = 0.03125$ **(b)** $h_{xfem}/L = 0.0625$

Fig. 12. Cells cut by the crack front.

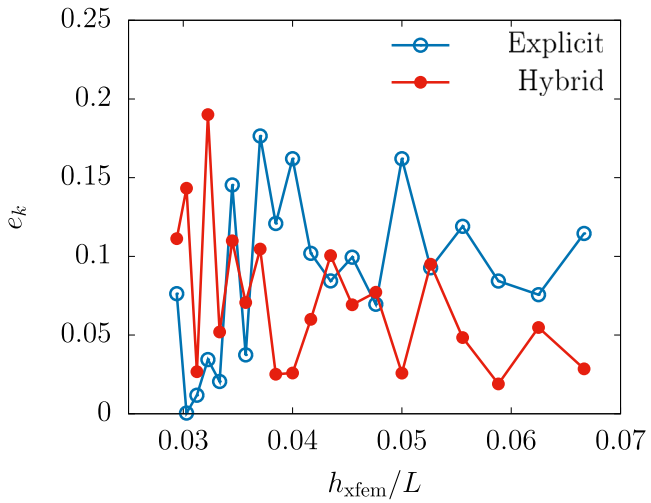

Fig. 13. Relative errors for different mesh sizes. ($e_k = \left|k_{\mathrm{I}} - k_{\mathrm{I}}^{\mathrm{ref}}\right| / k_{\mathrm{I}}^{\mathrm{ref}}$).

$$\left[u_\theta(\theta)\right] = \frac{-c}{2\sin\theta}\int_\theta^\alpha \frac{\psi(t)\sin t}{\sqrt{2\cos\theta - 2\cos t}}\,\mathrm{d}t, \quad 0 \le \theta < \alpha, \tag{34}$$

where the spherical cap is represented by $r = c$, $0 \le \theta < \alpha$ and $0 \le \phi < 2\pi$. In this case, $c \equiv 0.2$, $\alpha \equiv \pi/4$. The expressions for $\varphi(t)$ and $\psi(t)$ are:

$$\varphi(t) = \eta\varphi_1(t) + (1-\upsilon)^{-1}\left\{\psi_0 h_0(t) + M_1 h_1(t) + M_2 h_2(t)\right\}, \tag{35}$$

$$\psi(t) = \eta\psi_1(t) + (1-\upsilon)^{-1}\left\{\psi_0 \ell_0(t) + M_1 \ell_1(t) + M_2 \ell_2(t)\right\}, \tag{36}$$

where $\eta = -4(1-\upsilon)p_0/(\pi\mu)$, υ is Poisson's ratio ($\upsilon \equiv 0.22$), p_0 is the tension along z-direction ($p_0 \equiv 1$), μ is the shear modulus ($\mu = \frac{E}{2(1+\upsilon)} = 409.836$) as $E = 1\times 10^3$, and functions are listed as follows:

$$\begin{aligned}
\varphi_1(t) &= 2A_1\sin\left(\frac{1}{2}t\right) + \frac{2}{3}B_1\sin\left(\frac{3}{2}t\right) + \frac{2}{5}C_1\sin\left(\frac{5}{2}t\right) + \upsilon^{-1}D_1\cosh\gamma t\sin\upsilon t + \gamma^{-1}E_1\sinh\gamma t\cos\upsilon t,\\
\psi_1(t) &= B_3\cos\left(\frac{3}{2}t\right) + C_3\cos\left(\frac{5}{2}t\right) + D_3\cosh\gamma t\cos\upsilon t + (\gamma\upsilon)^{-1}E_3\sinh\gamma t\sin\upsilon t,\\
h_0(t) &= -\frac{1}{8}\left\{\sin\left(\frac{3}{2}t\right) + (3-4\upsilon)\cosh\gamma t\sin\upsilon t + \frac{1}{2}\gamma^{-1}\left(1+6\upsilon-8\upsilon^2\right)\sinh\gamma t\cos\upsilon t\right\},\\
h_1(t) &= -\frac{1}{32}\left\{(3+8\upsilon)\sin\left(\frac{3}{2}t\right) + (13-24\upsilon)\cosh\gamma t\sin\upsilon t + \frac{1}{2}\gamma^{-1}\left(51-14\upsilon-48\upsilon^2\right)\sinh\gamma t\cos\upsilon t\right\},\\
h_2(t) &= \frac{1}{2}\delta_2\left\{\sin\left(\frac{3}{2}t\right) - \cosh\gamma t\sin\upsilon t + \frac{1}{2}\gamma^{-1}(1-2\upsilon)\sinh\gamma t\cos\upsilon t\right\},\\
\ell_0(t) &= \frac{1}{3}\left\{\cos\left(\frac{3}{2}t\right) + (2-3\upsilon)\cosh\gamma t\cos\upsilon t - \frac{1}{2}\gamma^{-1}\left(3+2\upsilon-6\upsilon^2\right)\sinh\gamma t\sin\upsilon t\right\},\\
\ell_1(t) &= \frac{1}{12}\left\{(3+8\upsilon)\left(\cos\left(\frac{3}{2}t\right) - \cosh\gamma t\cos\upsilon t\right) - \frac{1}{2}\gamma^{-1}\left(48-3\upsilon-56\upsilon^2\right)\sinh\gamma t\sin\upsilon t\right\},\\
\ell_2(t) &= -\frac{4}{3}\delta_2\left\{\cos\left(\frac{3}{2}t\right) - \cosh\gamma t\cos\upsilon t + \frac{1}{2}(\upsilon/\gamma)\sinh\gamma t\sin\upsilon t\right\},
\end{aligned}$$

where

$$\begin{aligned}
&A_1 = \frac{1}{16(1+\upsilon)}, \quad B_1 = \frac{-3}{16(1-\upsilon)}, \quad C_1 = \frac{25}{4(7-5\upsilon)}, \quad D_1 = \frac{-\upsilon\left(3+5\upsilon-10\upsilon^2\right)}{4\left(1-\upsilon^2\right)(7-5\upsilon)},\\
&E_1 = \frac{13-25\upsilon-6\upsilon^2+20\upsilon^3}{8\left(1-\upsilon^2\right)(7-5\upsilon)}, \quad B_3 = -\frac{16}{9}B_1, \quad C_3 = -\frac{24}{25}C_1, \quad D_3 = \frac{11-13\upsilon}{3(1-\upsilon)(7-5\upsilon)},\\
&E_3 = \frac{\upsilon(1-2\upsilon)(15-17\upsilon)}{6(1-\upsilon)(7-5\upsilon)}, \gamma = \frac{1}{2}\sqrt{3-4\upsilon^2}, \quad \delta_2 = \frac{3}{16}(1-8\upsilon).
\end{aligned}$$

The coefficients of M_1, M_2 and ψ_0 are the solution of the following linear system:

$$\sum_{j=1}^{3} A_{ij}x_j = c_i, \quad i = 1,2,3,$$

where $x_1 = M_1, x_2 = M_2, x_3 = \psi_0$ and

$$\begin{aligned}
&c_1 = (1-\upsilon)\eta\int\varphi_1\,\mathrm{d}t, \quad c_2 = (1-\upsilon)\eta\int\left(\varphi_1\cos t + \psi_1\sin t\right)\mathrm{d}t, \quad c_3 = -(1-\upsilon)\eta\int\psi_1\cos\frac{1}{2}t\,\mathrm{d}t,\\
&A_{11} = 1-\upsilon-\int h_1\,\mathrm{d}t, \quad A_{12} = -\int h_2\,\mathrm{d}t, \quad A_{13} = -\int h_0\,\mathrm{d}t,\\
&A_{21} = -\int\left(h_1\cos t + \ell_1\sin t\right)\mathrm{d}t, \quad A_{22} = 1-\upsilon-\int\left(h_2\cos t + \ell_2\sin t\right)\mathrm{d}t,\\
&A_{23} = -\int\left(h_0\cos t + \ell_0\sin t\right)\mathrm{d}t,\\
&A_{31} = \int\ell_1\cos\left(\frac{1}{2}t\right)\mathrm{d}t, \quad A_{32} = \int\ell_2\cos\left(\frac{1}{2}t\right)\mathrm{d}t, \quad A_{33} = \int\ell_0\cos\left(\frac{1}{2}t\right)\mathrm{d}t,
\end{aligned}$$

and all the integrals are over the range $0 \le t \le \alpha$. We thus can compute the analytical solutions of $\left[u_r(\theta)\right]$ and $\left[u_\theta(\theta)\right]$. Fig. 14 compares the displacement jumps for different methods at various mesh sizes. We can see that the proposed method (labeled as "hybrid") is more accurate than the method requiring transposition matrix (labeled as "explicit") both for $\left[u_r(\theta)\right]$ and $\left[u_\theta(\theta)\right]$.

6. Conclusion

Using the X-FEM to model non-planar discontinuities confronts challenges to compute gradients of enriching functions since the transformations matrix connecting the global and local coordinate systems are sensitive to the normal, conormal, and tangent vectors along crack fronts. In this work, we proposed a novel hybrid representation by setting level sets to an independent grid with hexahedra meshes. The gradients of level sets are computed by the finite difference method and then interpolated to the integration

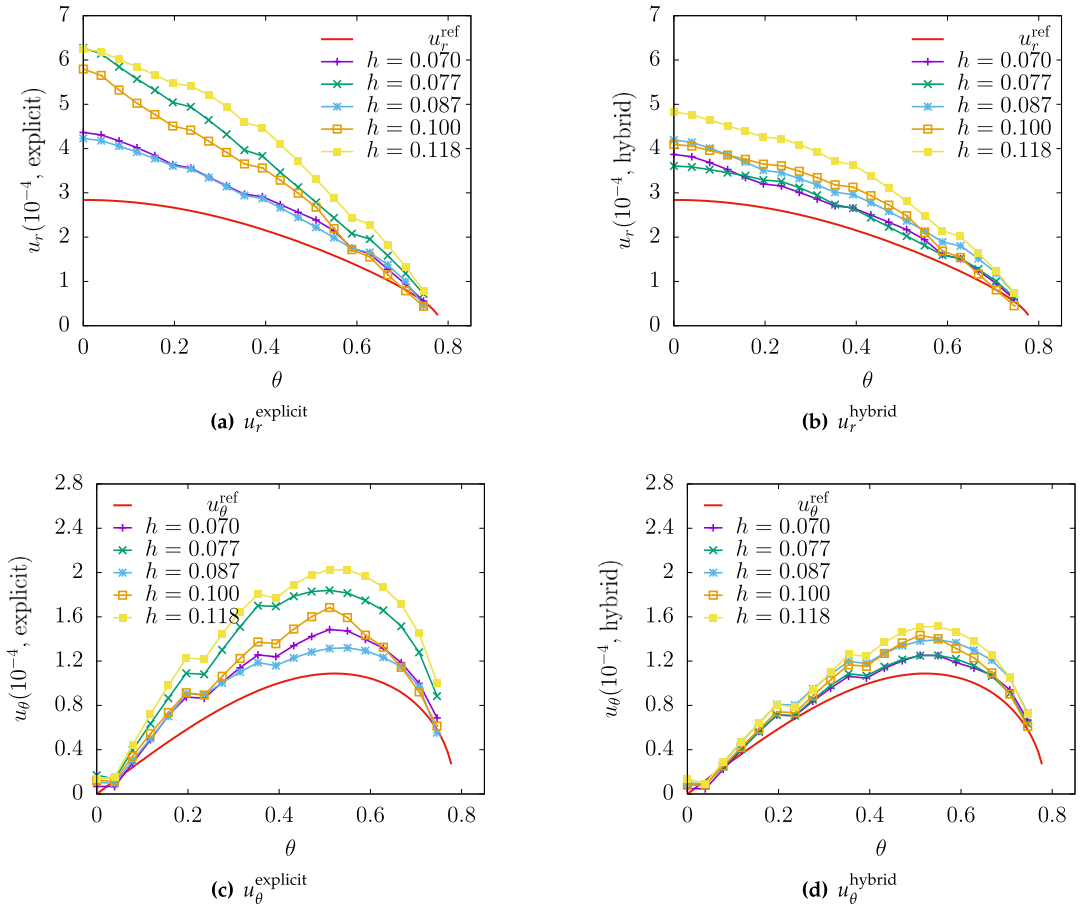

(a) u_r^{explicit} **(b)** u_r^{hybrid}

(c) $u_\theta^{\text{explicit}}$ **(d)** u_θ^{hybrid}

Fig. 14. Comparisons of the displacement jump for different numerical solutions (explicit and hybrid) and analytical solutions (subscripts with ref).

points of the X-FEM to compute the gradients of enriching functions abandoning computing the local coordinate systems at the fronts of the cracks. It is found that the proposed method are identical to the explicit representation for planar cracks, but exhibit more accurate for the non-planar cracks, especially for coarse meshes. In this work, we consider embedded cracks in isotropic homogeneous materials. For interface cracks and cracks in anisotropic media, they can be modeled by using different enriching functions in the framework of the X-FEM. These enriching functions are also functions of r and θ, therefore the gradients of these functions can be computed by the chain rule and gradients of level sets in the same manner. It should be pointed out that the proposed method is based on level sets reproducing the explicit cracks. For some cases where the level set function may be an "over-smoothed" approximation to the crack geometry, e.g. the de facto "zigzag" feature of fatigue crack geometry, the explicit representation requiring the transformation matrix is still the best choice, while refining the crack tips is necessary to alleviate errors. As the future work, we may extend our model to consider multiple cracks.

Declaration of competing interest

The authors declare the following financial interests/personal relationships which may be considered as potential competing interests: Chuanqi Liu reports financial support was provided by National Natural Science Foundation of China. Yujie Wei reports financial support was provided by National Natural Science Foundation of China.

Data availability

Data will be made available on request.

Acknowledgments

Y. Wei acknowledges support from the National Natural Science Foundation of China (NSFC) (No. 11988102, No. 11790291), and C. Liu thanks support from NSFC (No. 12172368) and the One Hundred Talents Program of Chinese Academy of Sciences (CAS).

Appendix A. Gradients of enriching functions

$$\frac{\partial B_1}{\partial r} = \frac{1}{2\sqrt{r}}\sin\frac{\theta}{2}, \quad \frac{\partial B_1}{\partial \theta} = \frac{\sqrt{r}}{2}\cos\frac{\theta}{2} \tag{A.1}$$

$$\frac{\partial B_2}{\partial r} = \frac{1}{2\sqrt{r}}\cos\frac{\theta}{2}, \quad \frac{\partial B_2}{\partial \theta} = -\frac{\sqrt{r}}{2}\sin\frac{\theta}{2} \tag{A.2}$$

$$\frac{\partial B_3}{\partial r} = \frac{1}{2\sqrt{r}}\sin\frac{\theta}{2}\sin\theta, \quad \frac{\partial B_3}{\partial \theta} = \frac{\sqrt{r}}{2}\cos\frac{\theta}{2}\sin\theta + \sqrt{r}\sin\frac{\theta}{2}\cos\theta \tag{A.3}$$

$$\frac{\partial B_4}{\partial r} = \frac{1}{2\sqrt{r}}\cos\frac{\theta}{2}\sin\theta, \quad \frac{\partial B_4}{\partial \theta} = -\frac{\sqrt{r}}{2}\sin\frac{\theta}{2}\sin\theta + \sqrt{r}\cos\frac{\theta}{2}\cos\theta \tag{A.4}$$

Appendix B. Coefficients in the reference solutions of lens crack

The definitions of the coefficients a_{ij} and b_{ij} occurring in (32) are listed as follows.

$$\begin{aligned}
a_{11} &= \tfrac{1}{3}\left(11\cos\tfrac{\alpha}{2} - \cos\tfrac{5\alpha}{2}\right)\\
a_{12} &= \sin\alpha\left(\kappa\sinh\gamma\alpha\cos\tfrac{\alpha}{m} + \rho\cosh\gamma\alpha\sin\tfrac{\alpha}{m}\right) + \cos\alpha\left(\mu\cosh\gamma\alpha\cos\tfrac{\alpha}{m} - \beta\sinh\gamma\alpha\sin\tfrac{\alpha}{m}\right)\\
a_{13} &= \sin\alpha\left(\kappa\cosh\gamma\alpha\sin\tfrac{\alpha}{m} - \rho\sinh\gamma\alpha\cos\tfrac{\alpha}{m}\right) + \cos\alpha\left(\mu\sinh\gamma\alpha\sin\tfrac{\alpha}{m} + \beta\cosh\gamma\alpha\cos\tfrac{\alpha}{m}\right)\\
a_{21} &= \cos\tfrac{3\alpha}{2}\\
a_{22} &= 2\left(\gamma\cosh\gamma\alpha\cos\tfrac{\alpha}{m} + \tfrac{1}{m}\sinh\gamma\alpha\sin\tfrac{\alpha}{m}\right)\\
a_{23} &= 2\left(\gamma\sinh\gamma\alpha\sin\tfrac{\alpha}{m} - \tfrac{1}{m}\cosh\gamma\alpha\cos\tfrac{\alpha}{m}\right)\\
a_{31} &= \tfrac{1}{3}(1+\cos\alpha)\sin\alpha\\
a_{32} &= \tfrac{m}{4(m-1)}\cos\tfrac{\alpha}{2}\left[\left(1-\tfrac{2}{m}\right)\sinh\gamma\alpha\cos\tfrac{\alpha}{m} + 2\gamma\cosh\gamma\alpha\sin\tfrac{\alpha}{m}\right]\\
&+\tfrac{m}{4(m-1)}\tfrac{2}{3}\sin\tfrac{\alpha}{2}\left[\left(1-\tfrac{4}{m}\right)\gamma\cosh\gamma\alpha\cos\tfrac{\alpha}{m} + \left(\tfrac{3}{2}+\tfrac{1}{m}-\tfrac{4}{m^2}\right)\sinh\gamma\alpha\sin\tfrac{\alpha}{m}\right]\\
a_{33} &= \tfrac{m}{4(m-1)}\cos\tfrac{\alpha}{2}\left[\left(1-\tfrac{2}{m}\right)\cosh\gamma\alpha\sin\tfrac{\alpha}{m} - 2\gamma\sinh\gamma\alpha\cos\tfrac{\alpha}{m}\right]\\
&+\tfrac{m}{4(m-1)}\tfrac{2}{3}\sin\tfrac{\alpha}{2}\left[\left(1-\tfrac{4}{m}\right)\gamma\sinh\gamma\alpha\sin\tfrac{\alpha}{m} - \left(\tfrac{3}{2}+\tfrac{1}{m}-\tfrac{4}{m^2}\right)\cosh\gamma\alpha\cos\tfrac{\alpha}{m}\right]\\
b_{11} &= \tfrac{1}{3}\cos\tfrac{3\alpha}{2} - \cos\tfrac{\alpha}{2}\\
b_{22} &= 3\cos\tfrac{\alpha}{2}\\
\beta &= \tfrac{4}{3}\tfrac{6m^2+m-8}{m(7m-8)}\\
\mu &= \tfrac{-4}{3}\tfrac{m-8}{7m-8}\gamma\\
\rho &= \tfrac{8m}{7m-8}\gamma\\
\kappa &= \tfrac{8(m-1)}{7m-8}
\end{aligned} \tag{B.1}$$

References

[1] Mian Xiao, Chuanqi Liu, WaiChing Sun, DP-MPM: Domain partitioning material point method for evolving multi-body thermal–mechanical contacts during dynamic fracture and fragmentation, Comput. Methods Appl. Mech. Engrg. 385 (2021) 114063.

[2] Ted Belytschko, Robert Gracie, Giulio Ventura, A review of extended/generalized finite element methods for material modeling, Modelling Simul. Mater. Sci. Eng. 17 (4) (2009) 043001.

[3] Jens M. Melenk, Ivo Babuška, The partition of unity finite element method: basic theory and applications, Comput. Methods Appl. Mech. Engrg. 139 (1–4) (1996) 289–314.

[4] Nicolas Moës, John Dolbow, Ted Belytschko, A finite element method for crack growth without remeshing, Internat. J. Numer. Methods Engrg. 46 (1) (1999) 131–150.

[5] Natarajan Sukumar, Nicolas Moës, Brian Moran, Ted Belytschko, Extended finite element method for three-dimensional crack modelling, Internat. J. Numer. Methods Engrg. 48 (11) (2000) 1549–1570.

[6] M. Stolarska, David L. Chopp, Nicolas Moës, Ted Belytschko, Modelling crack growth by level sets in the extended finite element method, Internat. J. Numer. Methods Engrg. 51 (8) (2001) 943–960.

[7] J.P. Pereira, C. Armando Duarte, Xiangmin Jiao, Three-dimensional crack growth with hp-generalized finite element and face offsetting methods, Comput. Mech. 46 (3) (2010) 431–453.

[8] J. Garzon, P. O'Hara, Carlos Armando Duarte, William G. Buttlar, Improvements of explicit crack surface representation and update within the generalized finite element method with application to three-dimensional crack coalescence, Internat. J. Numer. Methods Engrg. 97 (4) (2014) 231–273.

[9] Guizhong Xiao, Longfei Wen, Rong Tian, Arbitrary 3D crack propagation with Improved XFEM: Accurate and efficient crack geometries, Comput. Methods Appl. Mech. Engrg. 377 (2021) 113659.

[10] Konstantinos Agathos, Giulio Ventura, Eleni Chatzi, Stéphane P.A. Bordas, Stable 3D XFEM/vector level sets for non-planar 3D crack propagation and comparison of enrichment schemes, Internat. J. Numer. Methods Engrg. 113 (2) (2018) 252–276.

[11] Thomas-Peter Fries, Malak Baydoun, Crack propagation with the extended finite element method and a hybrid explicit-implicit crack description, Internat. J. Numer. Methods Engrg. 89 (12) (2012) 1527–1558.

[12] Anthony Gravouil, Nicolas Moës, Ted Belytschko, Non-planar 3D crack growth by the extended finite element and level sets—Part II: Level set update, Internat. J. Numer. Methods Engrg. 53 (11) (2002) 2569–2586.

[13] Marc Duflot, A study of the representation of cracks with level sets, Internat. J. Numer. Methods Engrg. 70 (11) (2007) 1261–1302.

[14] Daniele Colombo, An implicit geometrical approach to level sets update for 3D non planar X-FEM crack propagation, Comput. Methods Appl. Mech. Engrg. 237 (2012) 39–50.

[15] M. Baydoun, T.P. Fries, Crack propagation criteria in three dimensions using the XFEM and an explicit-implicit crack description, Int. J. Fract. 178 (1) (2012) 51–70.

[16] James Albert Sethian, Level Set Methods and Fast Marching Methods: Evolving Interfaces in Computational Geometry, Fluid Mechanics, Computer Vision, and Materials Science, Vol. 3, Cambridge University Press, 1999.

[17] Stanley Osher, Ronald P. Fedkiw, Level set methods: an overview and some recent results, J. Comput. Phys. 169 (2) (2001) 463–502.

[18] Alireza Sadeghirad, David L. Chopp, Xiang Ren, Eugene Fang, Jim Lua, A novel hybrid approach for level set characterization and tracking of non-planar 3D cracks in the extended finite element method, Eng. Fract. Mech. 160 (2016) 1–14.

[19] Rong Tian, Longfei Wen, Lixiang Wang, Three-dimensional improved XFEM (IXFEM) for static crack problems, Comput. Methods Appl. Mech. Engrg. 343 (2019) 339–367.

[20] A.G. Sanchez-Rivadeneira, N. Shauer, B. Mazurowski, C.A. Duarte, A Stable Generalized/eXtended p-hierarchical FEM for three-dimensional linear elastic fracture mechanics, Comput. Methods Appl. Mech. Engrg. (ISSN: 0045-7825) 364 (2020) 112970, http://dx.doi.org/10.1016/j.cma.2020.112970, URL https://www.sciencedirect.com/science/article/pii/S0045782520301535.

[21] P. Gupta, Carlos Armando Duarte, A. Dhankhar, Accuracy and robustness of stress intensity factor extraction methods for the generalized/eXtended Finite Element Method, Eng. Fract. Mech. 179 (2017) 120–153.

[22] Xiangmin Jiao, Face offsetting: A unified approach for explicit moving interfaces, J. Comput. Phys. 220 (2) (2007) 612–625.

[23] J.P. Pereira, C.A. Duarte, X. Jiao, D. Guoy, Generalized finite element method enrichment functions for curved singularities in 3D fracture mechanics problems, Comput. Mech. 44 (1) (2009) 73–92.

[24] Guang-Shan Jiang, Danping Peng, Weighted ENO schemes for Hamilton–Jacobi equations, SIAM J. Sci. Comput. 21 (6) (2000) 2126–2143.

[25] James R. Rice, A path independent integral and the approximate analysis of strain concentration by notches and cracks, 1968.

[26] Brian Moran, C.F. Shih, Crack tip and associated domain integrals from momentum and energy balance, Eng. Fract. Mech. 27 (6) (1987) 615–642.

[27] M. Stern, E.B. Becker, R.S. Dunham, A contour integral computation of mixed-mode stress intensity factors, Int. J. Fract. 12 (3) (1976) 359–368.

[28] Barna A. Szabo, I. Babuška, Computation of the amplitude of stress singular terms for cracks and reentrant corners, in: Fracture Mechanics: Nineteenth Symposium, ASTM International, 1988.

[29] Ivo Babuška, Anthony Miller, The post-processing approach in the finite element method—Part 2: The calculation of stress intensity factors, Internat. J. Numer. Methods Engrg. 20 (6) (1984) 1111–1129.

[30] Leslie Banks-Sills, Itai Hershkovitz, Paul A. Wawrzynek, Rami Eliasi, Anthony R. Ingraffea, Methods for calculating stress intensity factors in anisotropic materials: Part I—z=0 is a symmetric plane, Eng. Fract. Mech. 72 (15) (2005) 2328–2358.

[31] Morteza Nejati, Adriana Paluszny, Robert W. Zimmerman, On the use of quarter-point tetrahedral finite elements in linear elastic fracture mechanics, Eng. Fract. Mech. 144 (2015) 194–221.

[32] P. Gupta, Carlos Armando Duarte, Coupled hydromechanical-fracture simulations of nonplanar three-dimensional hydraulic fracture propagation, Int. J. Numer. Anal. Methods Geomech. 42 (1) (2018) 143–180.

[33] Markus Schätzer, Thomas-Peter Fries, Stress intensity factors through crack opening displacements in the XFEM, in: Advances in Discretization Methods, Springer, 2016, pp. 143–164.

[34] F.L. Stazi, Elisa Budyn, Jack Chessa, Ted Belytschko, An extended finite element method with higher-order elements for curved cracks, Comput. Mech. 31 (1) (2003) 38–48.

[35] J.P. Pereira, C.A. Duarte, D. Guoy, X. Jiao, hp-Generalized FEM and crack surface representation for non-planar 3-D cracks, Internat. J. Numer. Methods Engrg. 77 (5) (2009) 601–633.

[36] A.G. Sanchez-Rivadeneira, N. Shauer, B. Mazurowski, C.A. Duarte, A stable generalized/extended p-hierarchical FEM for three-dimensional linear elastic fracture mechanics, Comput. Methods Appl. Mech. Engrg. 364 (2020) 112970.

[37] Varun Gupta, Dae-Jin Kim, C. Armando Duarte, Analysis and improvements of global–local enrichments for the generalized finite element method, Comput. Methods Appl. Mech. Engrg. 245 (2012) 47–62.

[38] Konstantinos Agathos, Eleni Chatzi, Stéphane P.A. Bordas, Stable 3D extended finite elements with higher order enrichment for accurate non planar fracture, Comput. Methods Appl. Mech. Engrg. 306 (2016) 19–46.

[39] Yongxiang Wang, Haim Waisman, Isaac Harari, Direct evaluation of stress intensity factors for curved cracks using Irwin's integral and XFEM with high-order enrichment functions, Internat. J. Numer. Methods Engrg. 112 (7) (2017) 629–654.

[40] Daniel Arndt, Wolfgang Bangerth, Denis Davydov, Timo Heister, Luca Heltai, Martin Kronbichler, Matthias Maier, Jean-Paul Pelteret, Bruno Turcksin, David Wells, The deal. II finite element library: Design, features, and insights, Comput. Math. Appl. 81 (2021) 407–422.

[41] Daniel Arndt, Wolfgang Bangerth, Bruno Blais, Marc Fehling, Rene Gassmöller, Timo Heister, Luca Heltai, Uwe Köcher, Martin Kronbichler, Matthias Maier, et al., The deal. II library, version 9.3, J. Numer. Math. 29 (3) (2021) 171–186.

[42] The CGAL Project, CGAL User and Reference Manual, 5.4 ed., CGAL Editorial Board, 2022, URL https://doc.cgal.org/5.4/Manual/packages.html.

[43] Michael Hemmer, Algebraic foundations, in: CGAL User and Reference Manual, 5.4 ed., CGAL Editorial Board, 2022, URL https://doc.cgal.org/5.4/Manual/packages.html#PkgAlgebraicFoundations.

[44] Kevin T. Chu, M. Prodanović, Level Set Method Library (LSMLIB), Tech. Rep., 2009.

[45] Ted L. Anderson, Fracture Mechanics: Fundamentals and Applications, CRC Press, 2017.

[46] Sylvie Pommier, Anthony Gravouil, Nicolas Moes, Alain Combescure, Extended Finite Element Method for Crack Propagation, John Wiley & Sons, 2013.

[47] Stéphane Bordas, Phu Vinh Nguyen, Cyrille Dunant, Amor Guidoum, Hung Nguyen-Dang, An extended finite element library, Internat. J. Numer. Methods Engrg. 71 (6) (2007) 703–732.

[48] Xiang Ren, Xuefei Guan, Three dimensional crack propagation through mesh-based explicit representation for arbitrarily shaped cracks using the extended finite element method, Eng. Fract. Mech. 177 (2017) 218–238.

[49] Pierre Alliez, Stéphane Tayeb, Camille Wormser, 3D fast intersection and distance computation, in: CGAL User and Reference Manual, 5.4 ed., CGAL Editorial Board, 2022, URL https://doc.cgal.org/5.4/Manual/packages.html#PkgAABBTree.

[50] Stanley Osher, Ronald P. Fedkiw, Level Set Methods and Dynamic Implicit Surfaces, Vol. 1, Springer, New York, 2005.

[51] Kyoungsoo Park, Jeronymo P. Pereira, C. Armando Duarte, Glaucio H. Paulino, Integration of singular enrichment functions in the generalized/extended finite element method for three-dimensional problems, Internat. J. Numer. Methods Engrg. 78 (10) (2009) 1220–1257.
[52] Eric B. Chin, Jean-Bernard Lasserre, Natarajan Sukumar, Modeling crack discontinuities without element-partitioning in the extended finite element method, Internat. J. Numer. Methods Engrg. 110 (11) (2017) 1021–1048.
[53] Chuanqi Liu, Jean H. Prévost, N. Sukumar, Modeling piecewise planar fault discontinuities without element-partitioning in 3D reservoir-geomechanical models, Int. J. Numer. Anal. Methods Geomech. 43 (2) (2019) 530–543.
[54] N. Sukumar, Extended finite element method, 2022, Website. http://dilbert.engr.ucdavis.edu/~suku/xfem/.
[55] M. Gosz, B. Moran, An interaction energy integral method for computation of mixed-mode stress intensity factors along non-planar crack fronts in three dimensions, Eng. Fract. Mech. 69 (3) (2002) 299–319.
[56] Daniel Bremberg, Jonas Faleskog, A numerical procedure for interaction integrals developed for curved cracks of general shape in 3-D, Int. J. Solids Struct. 62 (2015) 144–157.
[57] Fang Shi, Jishan Liu, A fully coupled hydromechanical XFEM model for the simulation of 3D non-planar fluid-driven fracture propagation, Comput. Geotech. 132 (2021) 103971.
[58] B. Mazurowski, A.G. Sanchez-Rivadeneira, N. Shauer, C.A. Duarte, High-order stable generalized/extended finite element approximations for accurate stress intensity factors, Eng. Fract. Mech. 241 (2021) 107308.
[59] Hiroshi Tada, Paul C. Paris, George R. Irwin, The stress analysis of cracks, in: Handbook, Vol. 34, Del Research Corporation, 1973.
[60] P.A. Martin, The spherical-cap crack revisited, Int. J. Solids Struct. 38 (26–27) (2001) 4759–4776.
[61] M.A. Martynenko, A.F. Ulitko, Stress state near the vertex of a spherical notch in an unbounded elastic medium, Sov. Appl. Mech. 14 (9) (1978) 911–918.